Effect of calcination temperature on electrochemical performance of niobium oxides/carbon composites

Effect of calcination temperature on electrochemical performance of niobium oxides/carbon composites

Haojie Fei[1*], Natalia Kazantseva[1], Viera Pechancova[2], Marek Jurca[1], David Skoda[1], Michal Urbanek[1], Pavel Urbanek[1], Michal Machovsky[1], Nikola Bugarova[3], and Petr Saha[2]

[1]Centre of Polymer Systems, Tomas Bata University in Zlín, 760 01 Zlín, Czech Republic

[2]University Institute, Tomas Bata University in Zlín, 760 01 Zlín, Czech Republic

[3]Polymer Institute, Slovak Academy of Sciences, Dúbravská cesta 9, 845 41 Bratislava, Slovakia

Address correspondence to E-mail: haojie@utb.cz

ABSTRACT

Orthorhombic niobium pentoxide (T-Nb2O5) possesses an intercalation pseudocapacitive behavior, which is a promising candidate of high-rate anodes for Li-ion capacitors. However, its low electric conductivity hinders the realization of this property. In our study, niobium oxides/carbon composites were prepared by calcinating a niobium peroxo-PAA complex (NbPAA) precursor to improve the electric conductivity. It has been found that the calcination temperature played an important role on the chemical compositions of obtained composites. A reduction phenomenon of niobium oxides by carbon was observed at high temperatures. At the medium temperature of 900 °C, the sample was composed of T-Nb_2O_5, monoclinic Nb2O5 (M-Nb_2O_5), amorphous carbon and niobium dioxide (NbO_2). Due to the high conductivity of carbon, semi-conductivity of NbO_2, and high specific capacity of M-Nb_2O_5, this sample exhibits a good specific capacity of 142 mAh g^{-1} (0.25 C) and a high-rate capability (capacity retention of 33.1%, 0.25 C to 25 C). It could be used as one of high-rate anodes for Li-ion capacitors.

Introduction

Rechargeable batteries and supercapacitors have been widely studied for the applications such as electronics, electrical vehicles, and stationary energy storage. Rechargeable batteries have a high energy density but low power density. Supercapacitors are the other way around. Developing one electrochemical energy storage system with both high energy and power densities as well as long cycling life has drawn massive attention **[1-3]**. Li-ion capacitors are one of most promising candidates, which consist of a high-capacity electrode (battery-type) and a high-rate capacitive electrode. It can surpass the energy density of conventional supercapacitors because of the higher capacity of battery-type electrode and overcome the power density limitation of batteries due to the presence of capacitive electrode **[4].**

The energy density could be improved through two approaches: capacity improvement and voltage expansion. Since the specific capacity of battery-type electrodes is many times higher than that of capacitive electrodes, the capacitance of Li-ion capacitors can approximately reach to twofold of that of symmetric supercapacitors. On the other hand, the electrolytes of Li-ion capacitors are Li-ion conducting organic electrolytes, which have a wider working potential than aqueous electrolytes. Moreover, in symmetric supercapacitors, the working voltage of full cell typically could not exceed its

electrode's maximum working potential range **[2,5]**. Therefore, the maximum specific capacitance stored in a full cell is only half of that of its electrode. By selecting proper battery-type electrode that works in a separated potential range, full capacitance of the capacitive electrode could be utilized, and the output voltage of the full-cell Li-ion capacitors can also be enlarged. It is well known as an asymmetric configuration.

The selection of battery-type electrodes for Li-ion capacitors is the key to achieve desired performances. Recently, many anode materials such as Ti-based oxides/compounds (TiO_2 and $Li_4Ti_5O_{12}$, etc.), silicon, Fe_3O_4, and intercalated carbon, and cathode materials of $LiNi_{0.5}Mn_{15}O_4$, $Li_3V_2(PO_4)_3$, spinel-$LiMn_2O_4$, Li_2-$CoPO_4F$, and their hybrids with various conducting carbon/polymers were investigated for Li-ion capacitors **[2]**. However, the balance in power capability between the sluggish lithium intercalation electrode and rapid capacitive electrode should be considered before choosing proper battery-type electrodes. Among them, $Li_4Ti_5O_{12}$ and Nb_2O_5 are two outstanding high-power anode materials [6-9]. Nb_2O_5 is worthy of notice because of its higher theoretical capacity (*200 mAh g^{-1}) than that of conventional $Li_4Ti_5O_{12}$ (~170 mAh g^{-1}). This property could be helpful in improving the energy density of Li-ion capacitors. Like $Li_4Ti_5O_{12}$, Nb_2O_5-based Li-ion capacitors working in the safe voltage range are free of the potential safety problems associated with the electrolyte decomposition, which can result in stable cycle life. In addition, Nb_2O_5-based Li-ion capacitors do not require the high-priced and inefficient prelithiation of anode materials, which is essential to achieve high energy density with stable cycle performance in the fabrication of commercial Li-ion capacitors **[10].** There are several crystalline Nb_2O_5. Orthorhombic Nb_2O_5(T-Nb_2O_5) is more favorable for the reversible Li intercalation compared with other structure of Nb_2O_5, resulting in a relatively better performance, especially cycle stability **[11-13].** However, further progress of Nb_2O_5 anodes for practical applications faces challenges due to their intrinsic poor electric conductivity (* 3 x 10-6 S cm^{-1}) **[14, 15]**.

In this study, we prepared a niobium peroxo-PAA complex (NbPAA) precursor through a modified Pechini method. Several composites were prepared by the carbonization of NbPAA precursor at different temperatures. PAA was used as the carbon source and stabilization agent for niobium oxides/carbon composites. Due to the strong bonding between niobium peroxo and carboxylic groups of PAA, the niobium oxides could be well dispersed in the carbon matrix, improving the electron transport. The impact of calcination temperature on the chemical compositions of these composites was studied. As a result, a reduction phenomenon of niobium oxides by carbon was observed at high temperatures. By choosing an appropriate temperature, this phenomenon could be used to improve electrochemical performance.

Experimental

Material preparation

Typically, 3 g of ammonium niobate(V) oxalate hydrate and 1.46 g of poly(acrylic acid) (PAA, average Mw 1800) were placed in a glass flask equipped with a magnetic stirrer. Then, 30 ml of hydrogen peroxide (30%) aqueous solution was added and stirred until the solids were totally dissolved and the solution turned to be clear. This solution was then heated and refluxed at 60 °C for 3 h. The transparent yellow solution turned to be blurry. Afterward, the solution was dried at 50 °C overnight and a yellow solid niobium peroxo-PAA complex (NbPAA) precursor was obtained. Finally, this obtained NbPAA precursor was ground and calcinated at various temperatures of 700 °C, 900 °C and 1100 °C for 2 h in an argon atmosphere at a heating rate of 3.3 °C min^{-1}. The obtained samples were named as NbPAA-700, NbPAA-900 and NbPAA-1100, respectively.

Structural and chemical characterization

The thermal decomposition of prepared NbPAA precursor was studied using thermogravimetric (TG) analysis (TA Q500, TA Instruments, USA). This measurement was carried out in a flow of N_2 from room temperature to 800 °C. The carbon contents in NbPAA-700, NbPAA-900 and NbPAA-1100 were also measured by TG analysis, by heating them from room temperature to 800 °C in an Air flow. The TG run was all conducted at a heating rate of 10 °C min^{-1}. The nanostructure and morphology characterization were investigated by scanning electron microscope (SEM, Nova Nano SEM 450, FEI Company, USA) and transmission electron microscopy (TEM, JEM 2100, JEOL, Japan). Au/Pd coating was applied before the SEM measurement. The powder XRD patterns were recorded on a Rigaku MiniFlex 600 diffractometer equipped with a CoK_α (λ = 1.7903 Å) radiation in a 2Θ range from 5°to 90°. The chemical compositions and binding energies of samples were studied by X-ray Photoelectron Spectroscopy (XPS, Hermo Scientific™ K-Alpha XPS system, Thermo Fisher Scientific, USA).

Electrochemical measurement

The active materials (NbPAA-700, NbPAA-900 and NbPAA-1100) were firstly ball milled. The working electrodes were fabricated by mixing 80 wt% of active material, 15 wt% of carbon black (Super P®) and 5 wt% of poly(acrylic acid) lithium slat (LiPAA, average Mw 450, 000), using water as the dispersing solvent. The prepared slurries were coated on copper foils and the electrodes were dried at 100 °C in vacuum overnight. The working electrodes were assembled in CR2032 coin cells, using Li metal chips as the counter and reference electrode, Celgard 2500 as the separator and 1 M LiPF6 in a mixture of ethylene carbonate (EC) and ethyl methyl carbonate (EMC) (EC/EMC, 1:1 v/v) as the electrolyte. Electrochemical measurements, such as cyclic voltammetry (CV) conducted at different scan rates, galvanostatic charge-discharge cycled between 1.1 and 3.0 V voltage window vs Li^+/Li and electrochemical impedance spectroscopy (EIS), were carried out using the BCS-810 battery cycler (BioLogic, France).

The reaction kinetic of NbPAA-900 was investigated using its CV curves at various scan rates. The peak current (*i*) has a relationship with the scan rate (*v*) according to the following equation:

$$i = \mathrm{a}\mathrm{v}^{b} \qquad (1)$$

Both a and b are adjustable parameters. In particular, b = 0.5 represents a diffusion-controlled faradaic intercalation process, while b = 1 indicates a capacitive behavior via a surface faradaic redox reaction. In order to distinguish the capacitive contribution from the current response, Eq. (1) is rewritten as

$$i(V) = k_1 v + k_2 v^{1/2} \qquad (2)$$

where k_1v and $k_2v^{1/2}$ can attribute to capacitive and diffusion-controlled contributions. For analytical purposes, Eq. (2) is rewritten as follows

$$i(V)/v^{1/2} = k_1 v^{1/2} + k_2 \qquad (3)$$

By plotting $v^{1/2}$ vs $i/v^{1/2}$, k_1 and k_2 can be derived from values of the slopes and intercepts. By knowing the values of k_1 and k_2, the ratio of capacitive contributions (k_1v) and diffusion-controlled contributions ($k_2v^{1/2}$) at different scan rate are obtained.

Results and discussion

Carboxylic groups in citric acid and oxalic acid are typically used to stabilize the Nb ion in the aqueous solution. In this way, niobium-based nanoparticles such as Nb_2O_5**[16]**, $LiNbO_3$**[17]** and $K_{0.5}Na_{0.5}$-NbO_3**[18]** have been prepared, which is well known as a modified Pechini method**[19, 20]**. However, due to the low molecular weight of citric acid and oxalic acid, it is hard to form a coating of amorphous carbon on the nanoparticles by carbonization. Here, we use PAA as the carbon source and the stabilization agent to prepare Nb_2O_5 nanoparticles within carbon matrix, leading to an increase in their electric conductivities.

Figure 1 illustrates the synthetic process of niobium compounds/carbon composites. Firstly, NbPAA precursor, where niobium peroxo are incorporated into PAA polymer network, is obtained via the oxidation of ammonium niobate(V) oxalate by H_2O_2 and the coordination between carboxylic groups and niobium peroxo **[18].** CO_2, NH_3 and O_2 are released due to the decomposition of oxalate by H_2O_2. Then, during the calcination, niobium-based nanoparticles are in situ generated and well dispersed in the carbon matrix. Different niobium compounds are formed at temperatures of 700 °C, 900 °C and 1100 °C, respectively. The compositions in these composites are listed in advance for a foresight based on the gained results of XRD analysis, which will be discussed afterward.

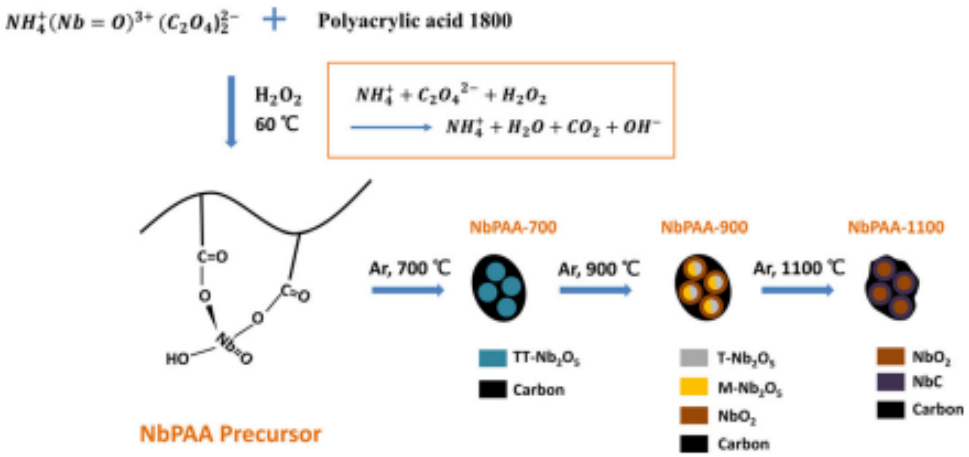

Figure 1 Schematic illustration of the preparation of NbPAA-700, NbPAA-900 and NbPAA-1100 composites, and their chemical compositions.

The thermal decomposition of NbPAA precursor was studied using TG analysis. The result is presented in Fig. 2. The overall weight loss is observed as high as 63%. The TG curve obviously shows three steps of weight loss. About 33.2% weight loss occurs between the temperature of 25 and 290 °C. It includes the elimination of water molecule before 150 °C, and the elimination of molecules of ammonia (NH_3), carbon dioxide (CO_2) and carbon monoxide (CO) between 160 and 290 °C, resulting from the decomposition of carboxylic groups in NbPAA precursor **[16].** This elimination leads to the formation of a mono(carboxyl)oxo-niobate complex, which shows a similar process as the one of (oxalato)oxo-niobate complex **[21].**

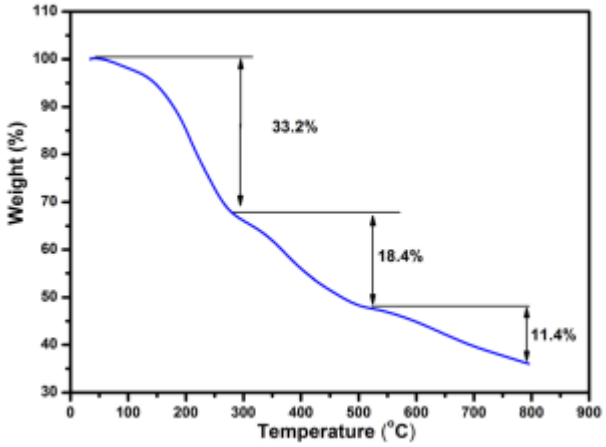

Figure 2 TG curve of NbPAA precursor under nitrogen atmosphere at 10 0C min^{-1}.

After this temperature, the further decomposition of this complex occurs with a weigh loss of 18.4% by forming CO. Meanwhile, the formation of Nb_2O_5 starts. The breakdown of the -$[CH_2\text{-}CH]_n$- occurs between the temperature of 500 °C and 600 °C. And a slight continuous weight loss is observed above 600 °C. It could be due to the formation of amorphous carbon by removing the remain groups such as -OH and -CH **[22].** The reduction of Nb_2O_5 by carbon is not significant below the temperature of 800 °C.

Nb_2O_5 generally has five different phases: amorphous Nb_2O_5 (a-Nb_2O_5), pseudohexagonal Nb_2O_5 (TT-Nb_2O_5), orthorhombic Nb_2O_5(T-Nb_2O_5), tetragonal Nb_2O_5 (B-Nb_2O_5) and monoclinc Nb_2O_5 (M-Nb_2O_5).**[23,24].** Due to their unique crystal structures, they perform different electrochemical behaviors in the lithium intercalation/deintercalation process. In general, T-Nb_2O_5 displays a pseudocapacitive performance and can enhance its rate capability on the premise of maintaining capacity **[9].** TT-Nb_2O_5 is an incompletely crystallized T-polymorph, which contained vacancies in the crystal texture. It has the similar XRD patterns and electrochemical behaviors with T-Nb_2O_5. M-Nb_2O_5 delivers the highest capacity (* 250 mAh g^{-1}) and a favorable rate capability among them. There are also other Nb-based compounds, such as niobium monoxide (NbO), niobium dioxide (NbO2), which could contribute to the electric conductivity and cycling ability of composites **[25]**.

Therefore, XRD analysis was applied to study the crystal structures of obtained niobium species/carbon composites. Figure 3a, b, and c shows the XRD patterns of the NbPAA-700 NbPAA-900 and NbPAA-1100 after the calcination at the corresponding temperatures. In all the samples, there are no significant diffraction peaks of carbon matrix, which indicates their amorphous property. For NbPAA-700, all the characteristic diffraction peaks could be indexed to TT-Nb_2O_5 (PDF#28-0317), which shows a different phase transition behavior to the samples in air, where orthorhombic phase could form at even lower temperature of 600 °C [9]. It seems that the formation of TT-Nb_2O_5 in NbPAA-700 could be caused by the lack of oxygen in Ar atmosphere, which creates more vacancies, leading to a difficult recrystallization. NbPPA-900 shows complex XRD diffraction patterns of three different phases including T-Nb_2O_5 (PDF#27-1003), M-Nb_2O_5 (PDF#26-0885) and NbO_2 (PDF#43-1043). It indicates the phase transition of TT-Nb_2O_5 to T-Nb_2O_5 and then T-Nb_2O_5 to M-Nb_2O_5 at the temperature of 900 °C. Moreover, the reduction of partial Nb_2O_5 to NbO_2 by carbon matrix is observed. The XRD patterns of NbPPA-1100 are the mixture of characteristic diffraction peaks of NbO2 and niobium carbide (NbC, PDF#38-1364), which confirms the severe reductions of Nb_2O_5 at this very high temperature.

TG analysis was conducted to study the content ratios of each composition in three samples. Figure 3d, e and f displays their TG curves in the air at a heating rate of 10 °C min^{-1}. For the one of NbPPA-700, it shows a platform in the beginning of heating due to the removing of water, then it has a steep drop above 370 °C, at which the carbon burning starts. However, for NbPPA-900 and NbPAA-1100, there are mass increases before the carbon removing because of the oxidation of NbO_2 in NbPPA-900, and NbO_2 and NbC in NbPAA-1100.

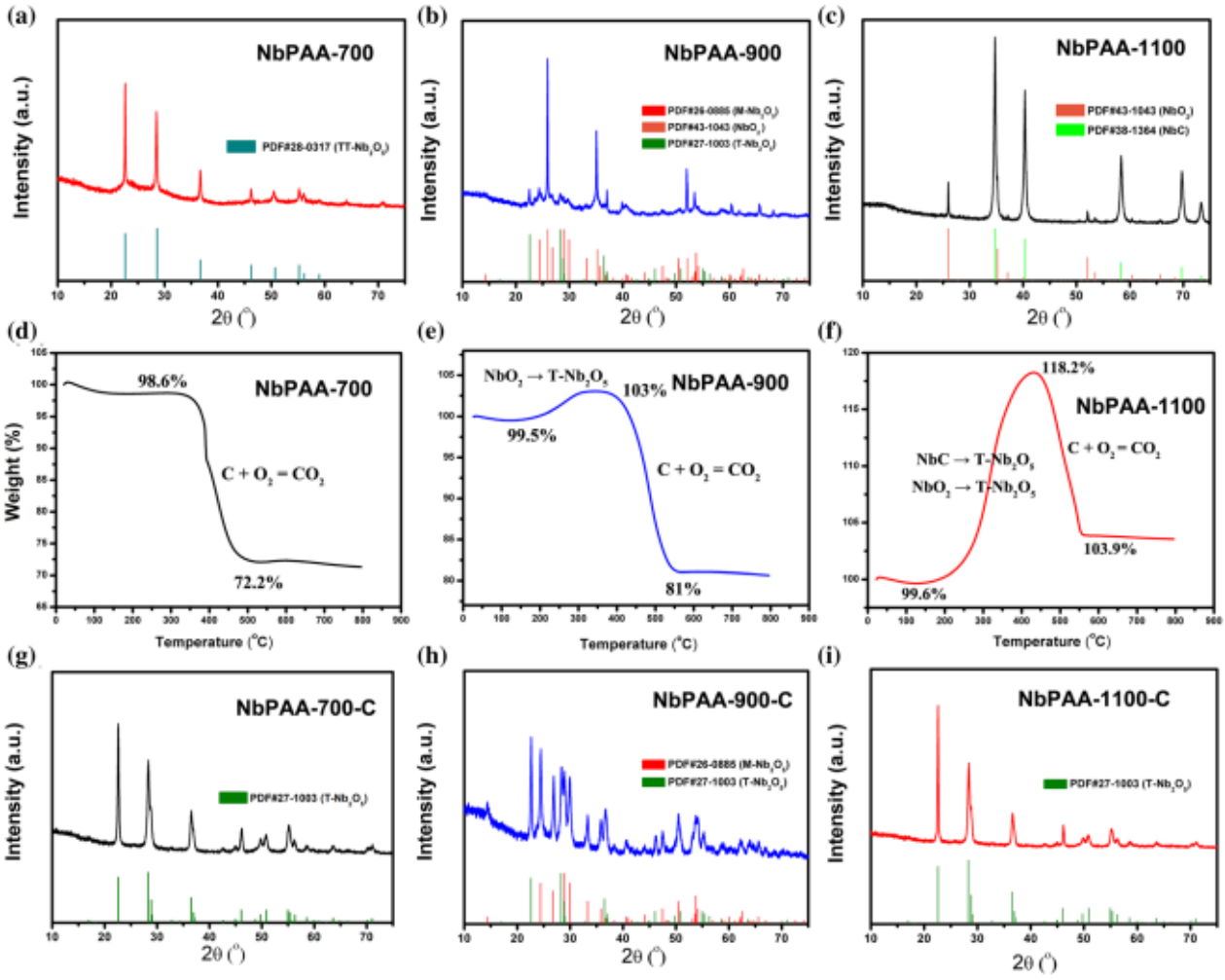

Figure 3 XRD patterns of a NbPAA-700, b NbPAA-900 and c NbPAA-1100; TG curves of d NbPAA-700, e NbPAA-900 and f NbPAA-1100 in an air flow at 10 °C min^{-1}; XRD patterns of g NbPAA-700-C, h NbPAA-900-C and i NbPAA-1100-C.

The samples were renamed as NbPAA-700-C, NbPAA-900-C and NbPAA-1100-C after removing the carbon matrix, respectively. Their phases were also investigated by XRD analysis, and the results are shown in Fig. 3g, h, and i. The phase of TT-Nb_2O_5 in NbPAA-700 becomes T-Nb_2O_5 due to the carbon removing was achieved by the thermal treatment in air. NbPAA-900-C is a mixture of T-Nb2O5 and M-Nb_2O_5. T-Nb_2O_5 comes from both the oxidation of NbO_2 and the initial T-Nb_2O_5 in NbPAA-900. M-Nb_2O_5 does not change during the removing of carbon since the phase transition of T-Nb_2O_5 to M-Nb_2O_5 occurs around 900 °C. NbPAA-1100-C is a pure T-Nb_2O_5, which is the result of oxidation of NbO_2 and NbC.

Based on the data from XRD and TG analysis, the content ratios of each composition are calculated and listed in Table 1. As you can see, the carbon content reduces from 26.4 to 14.3% when the temperature increases due to the further decomposition of carbon precursor and the reduction of niobium oxides by carbon. Meanwhile, the amount of NbO_2 increases upon the increasing temperature. In NbPAA-900, there are four different compositions, which could play their own unique advantage in the improvement of electrochemical performance. The optimization of content ratios of each composition could be done by adjusting the calcination temperature and heating time.

The morphological changes of NbPAA precursor at different temperatures were monitored by SEM. The results are shown in Fig. 4a, b and c. It is obvious to see that the prismatic structure of particles becomes cracked after the calcination. Higher temperature applied, more smaller particles can be observed, resulting from the decomposition of carbon precursor and the reduction reaction between carbon and niobium species within the increasing calcination temperature. After the removing of carbon in the air at 600 °C, the nanoparticles appear as shown in Fig. 4e, f and g. Although there are phase transitions and chemical reactions during the carbon removing, the consistent shapes of aggregated particles before and after the carbon removing indicates the obtained nanostructure should be transformed from the nanoparticles in the carbon matrix.

In order to directly observe the change of nanostructure inside the composites, TEM measurement was conducted and the results are shown in Fig. 5. As depicted in Fig. 5a, very small nanocrystals are well dispersed in the carbon matrix, benefiting from the strong bond between niobium peroxo complex and PAA in NbPAA precursor. Then, the size of nanoparticles becomes larger and they agglomerate as shown in Fig. 5b, which indicates the phase transition and crystal growth in NbPAA-900. And as seen in Fig. 5c, NbPAA-1100 has the largest particle size within agglomerates and the lowest amount of carbon. These results show that the significant reactions take place within the increase in calcination temperatures.

Figure 6a, b and c shows the full scan elemental survey of NbPAA-700, NbPAA-900 and NbPAA-1100, confirming their elemental compositions with the presence of the peaks of O, C and Nb. Figure 6d, e and f presents the C 1 s peaks of three samples. The peaks were deconvoluted into several peaks at different binding energies. Three main peaks (sp^2 CC bonding at 284.3 eV, sp^3 C-C bonding at 284.6 eV, C-O group at 285.9 eV) are identified. It is observed that by increasing the calcination temperature, the intensity of the sp^3 and C-O peaks decreases, while the sp^2 peak increases.

Table 1 The summary of the properties of NbPAA-700, NbPAA-900 and NbPAA-1100

Samples	Components	Percentage (%)	Specific capacity (mAh g^{-1}, at 0.1 A g^{-1})	Rate performance (0.05 to 5 A g^{-1})	Cycling (0.2 A g^{-1}, 200 cycles)
NbPAA-700	C	26.4%	87	12.3%	116%
	TT-Nb_2O_5	72.2%			
NbPAA-900	C	22%	129	33.1%	81.6%
	T-Nb_2O_5 & M-Nb_2O_5	22.8%			
	NbO_2	54.6%			
NbPAA-1100	C	14.3%	29	19.5%	80.2%
	NbO_2	78.5%			
	NbC	16.8%			

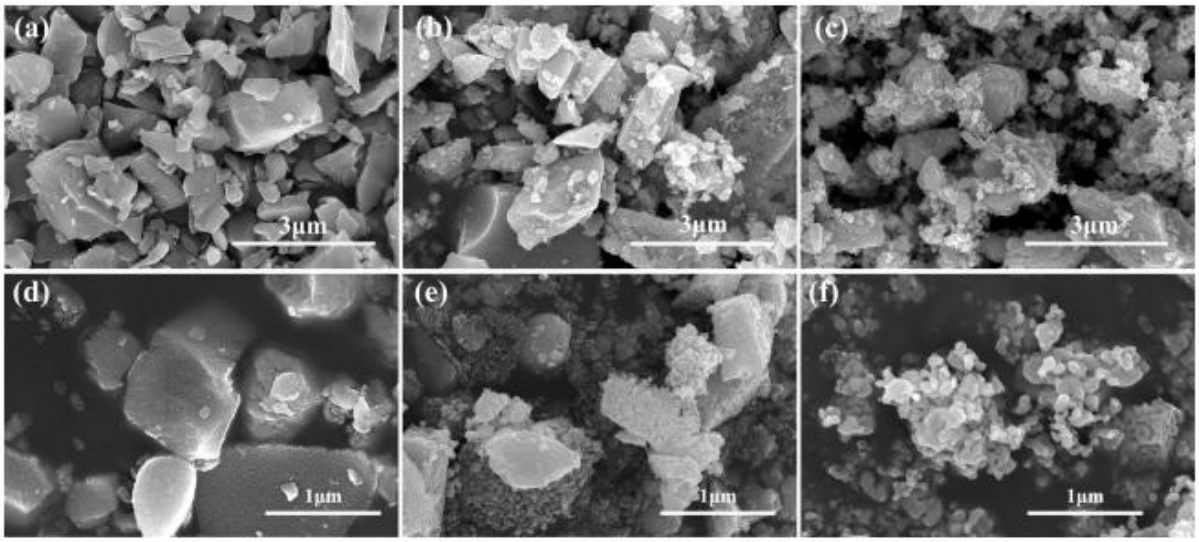

Figure 4 SEM images of a NbPAA-700, b NbPAA-900, c NbPAA-1100, g NbPAA-700-C, h NbPAA-900-C and i NbPAA-1100-C.

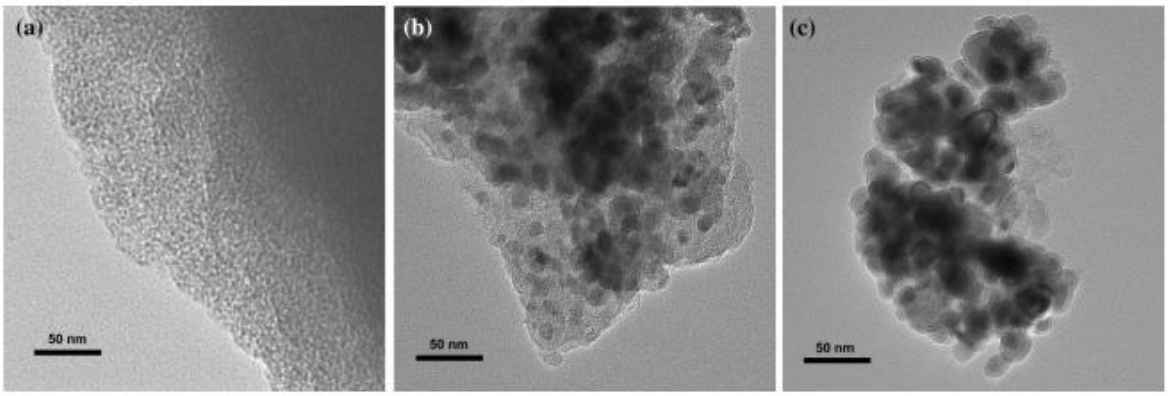

Figure 5 TEM images of a NbPAA-700, b NbPAA-900 and c NbPAA-1100.

The ratio of sp^3 carbon atoms to sp^2 carbon atoms is 3:2 in NbPAA-700, 3:8 in NbPAA-900 and 1:4 in NbPAA-1100, respectively. It indicates the graphitization of carbon matrix increases with the elevated calcination temperature. Graphitized carbon in the amorphous carbon matrix and porous graphitized carbon shell on the metal oxides can increase the electric conductivity without hindering the ionic transport **[26-28].** Finally, the carbide peak is observed in NbPAA-1100, which comes from NbC. Figure 6g, h and i displays the Nb 3d peaks of three samples. It is clear to see the Nb $3d_{5/2}$ and $3d_{3/2}$ peaks are all ascribed to Nb2O5 in NbPAA-700. And in NbPAA-900, they come from Nb2O5 and NbO2. These obtained composition information inside the samples are corresponding to the results of XRD. However, in NbPAA-1100, besides the peaks from NbO_2 and NbC, these peaks from NbO and Nb_2O_5 are also observed and even have much stronger intensities. According to the results of XRD, in which the diffraction patterns of NbO and Nb_2O_5 are not visible. It is reasonable to conclude that the oxidation of NbO_2 and NbC occurs in the air but only on their surface, considering that the XPS technique is mainly sensitive to the surface element species.

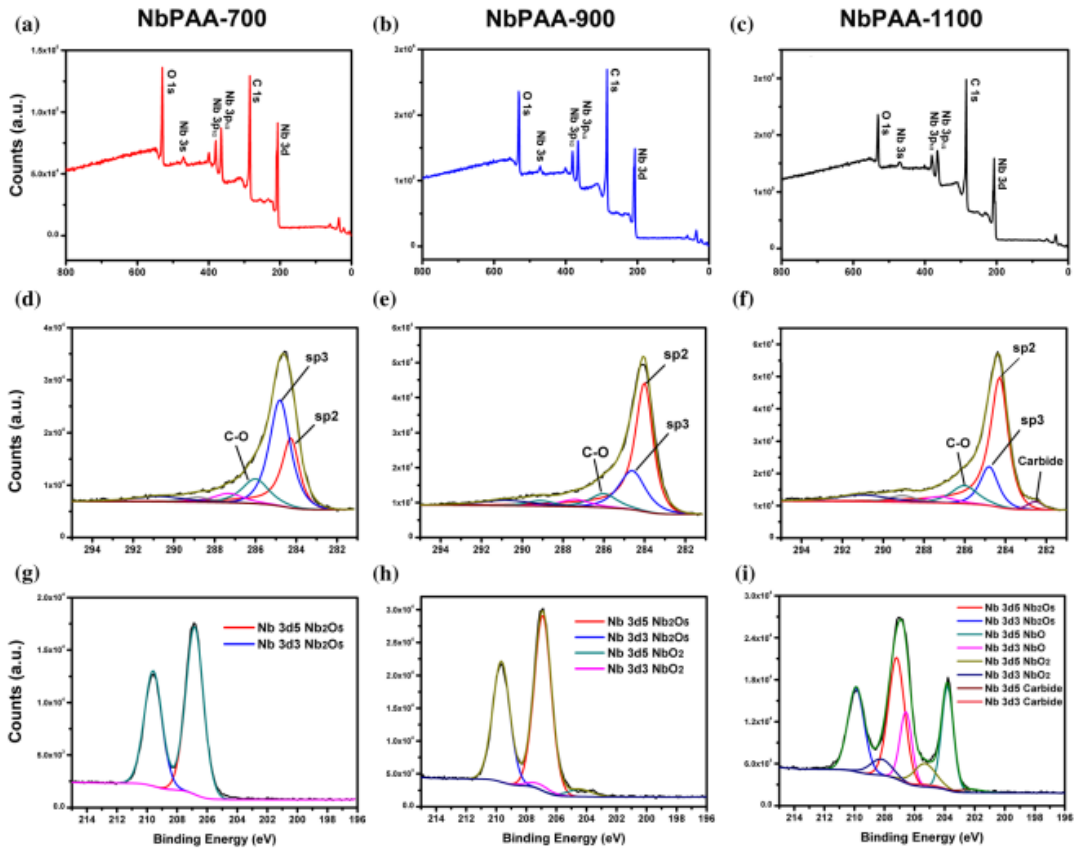

Figure 6 Survey, C 1 s and Nb 3d XPS spectra of (a, d, g) NbPAA-700, (b, e, h) NbPAA-900 and (c, f, i) NbPAA-1100, respectively.

CR2032 coin cells with Li chips as the counter and reference electrode were used to evaluate the electrochemical performance of samples. Figure 7a, b and c shows the first five cycles of voltammetry of NbPAA-700, NbPAA-900 and NbPAA-1100 at a scan rate of 0.1 mV s^{-1}, respectively. After the first cycle, the CV curves of each sample almost coincide in the next four cycles, which indicates the samples be well immersed in the electrolyte and have a good stability. The CV curves of NbPAA-700 exhibit an intercalation pseudocapacitive behavior, which is commonly observed in the phases of T-Nb_2O_5 and TT-Nb_2O_5.**[13, 29]** In Fig. 7b, the CV curves of NbPAA-900 show a cathodic (lithiation) peak at 1.6 V, and an anodic (delithiation) peak at 1.7 V, which are related to the redox couple of Nb^{5+}/Nb^{4+}. It is the faradic behavior of M-Nb_2O_5. Moreover, it has a quite large rectangle head in the potential range between 1.1 V and 1.5 V. Its current density at this range compared to the one of cathodic or anodic peak is considerably larger **[30].** It indicates the capacity in NbPAA-900 should be a combination of intercalation pseudo-capacitance of T-Nb2O5 and faradic capacity of M-Nb_2O_5. The CV curves of NbPAA-1100 show a rectangle shape in the whole range of working potential with a pair of weak redox peaks around 1.6 V. It could be integration of a double layer capacitive and a surface redox pseudocapacitive behavior. NbO_2 and NbC do not significantly contribute to the capacity of this sample due to the low theoretic specific capacity **[25, 31].**

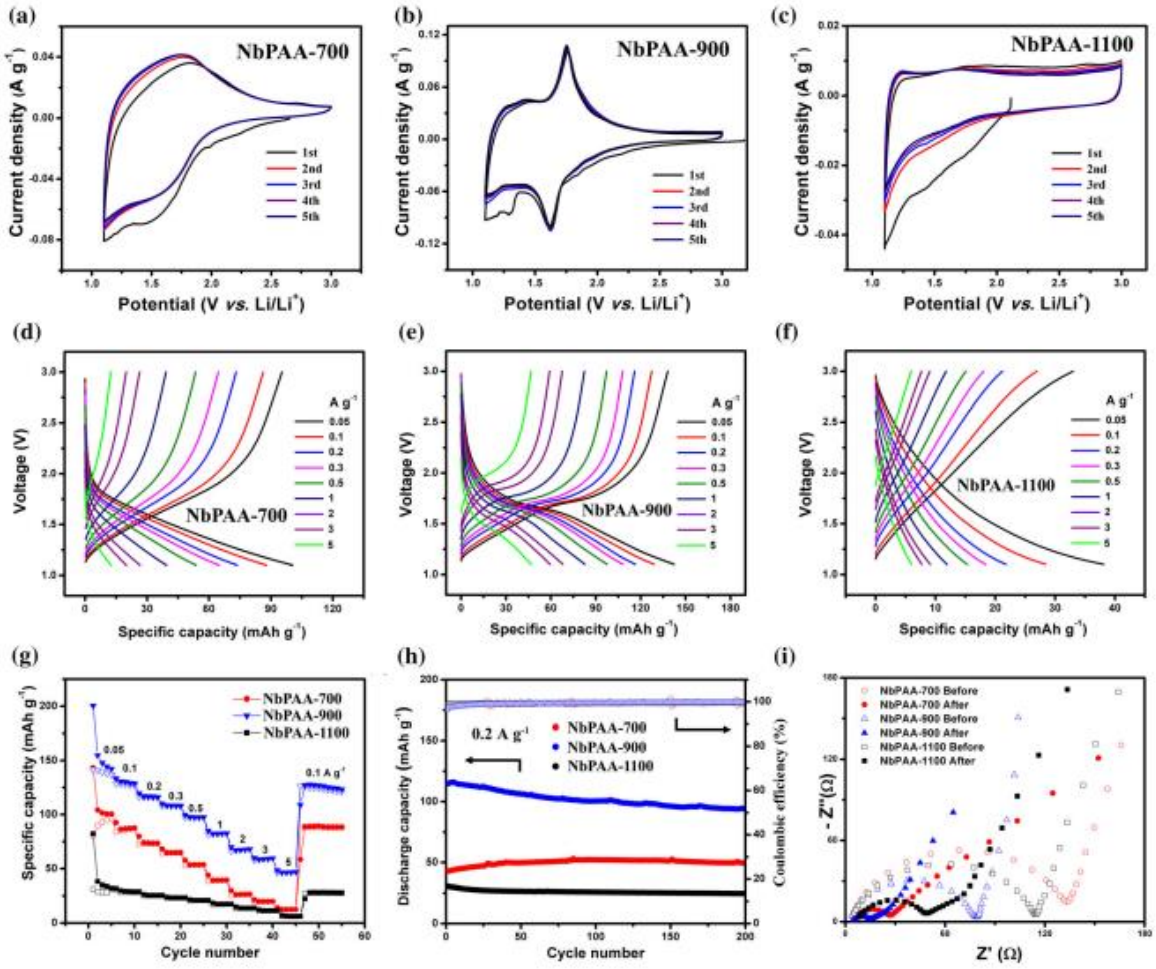

Figure 7 Electrochemical performance of NbPAA-700, NbPAA-900 and NbPAA-1100: a, b, c Cyclic voltammetry curves for the first 5 cycles; d, e, f Galvanostatic discharge/charge profiles at different current densities; g Rate performance; h Cycling performance at a current density of 0.2 A g^{-1} for 200 cycles, i Nyquist plots before and after cycling.

Figure 7d, e and f shows the galvanostatic discharge/charge profiles for the samples at different current densities. Their behaviors are consistent with the one of CV curves. For instance, there is a platform around 1.75 V in the discharge/charge profiles of NbPAA-900, which is ascribed to the redox peaks in the CV curves. And the profiles of NbPAA-700 and NbPAA-1100 are linear due to pseudocapacitive behaviors. The discharge specific capacity of NbPAA-900 is 142 mAh g^{-1} at 0.05 A g-1, which is higher than that of NbPAA-700 (100 mAh g^{-1}) and NbPAA-1100 (38 mAh g^{-1}). Since the prepared samples are used as the high-rate anode for Li-ion capacitors, higher current densities were applied. The highest current density is 5 A g^{-1}, which is 25 C based on the theoretical specific capacity of 200 mAh g^{-1}. The discharge and charge specific capacities upon various current densities are illustrated in Fig. 7g. As can be seen, the capacity gets reversible after the first five cycles at 0.05 A g-1. For all the samples, the specific capacity decreases when the current density increases. The retention ratios are 12.3%, 33.1% and 19.5% for NbPAA-700, NbPAA-900 and NbPAA-1100, respectively. The electric conductivity has a significant effect on the rate capability of electrode materials. In NbPAA-700 and NbPAA-1100, the higher graphitization of carbon matrix and the semi-conductivity of NbO_2 enhance their electron transport, resulting in a better rate capability.

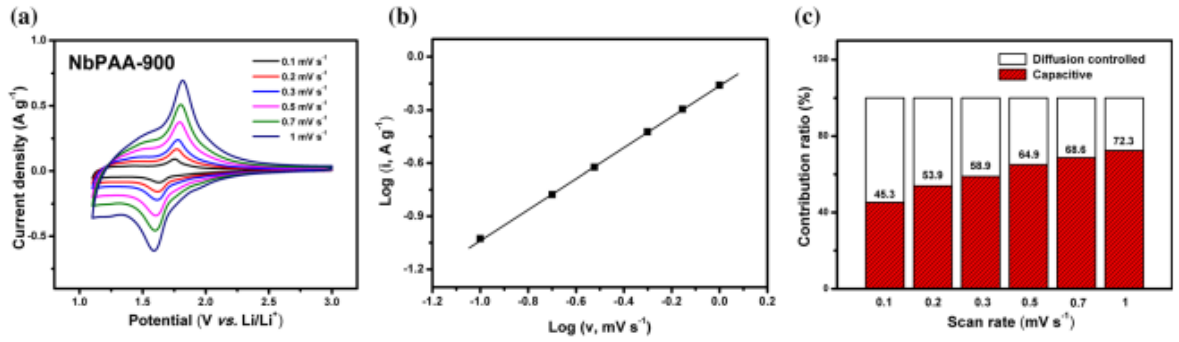

Figure 8 a Cyclic voltammetry curves of NbPAA-900 at different scan rates; b Determination of corresponding b-value of anodic peaks and c contribution ratios of the capacitive and diffusion-controlled capacity at various scan rates.

Moreover, despite the faradic reaction of the M-Nb_2O_5, its rate capacity is better than TT-Nb_2O_5 and T-Nb_2O_5. Therefore, NbPAA-900 exhibits the best rate capability, as well as the highest specific capacity.

Besides the specific capacity and high-rate capability, the coulombic efficiency and cycling stability are another two key parameters for commercial applications of the anode materials. The cycling tests start by five cycles at 0.05A g_{-1} and then continue 200 cycles at 0.2 A g_{-1}. The results are shown in Fig. 7h. The initial coulombic efficiencies of the NbPAA-700, NbPAA-900 and NbPAA-1100 are 39.8%, 71.7% and 42.9%, respectively. The coulombic efficiency of all samples increases to 99.2% after 10 cycles and keeps at this level for the rest cycles. The capacities on the dependence of cycle times are also shown in Fig. 7h. NbPAA-700 shows a good cycling stability after the stabilization of first 25 cycles, while the main decline of capacity of NbPAA-1100 occurs at the first 20 cycles, then it keeps almost the same. However, the capacity of NbPAA-900 continually deceases with a slight slope. After 200 cycles, the retention ratio of the capacity is about 81.6%. It is due to the low cycling stability of M-Nb_2O_5.

EIS results before and after the cycling are presented in Fig. 7i. There is no interfacial layer resistance at high frequency observed, which implies the solid electrolyte interphase does not form at high potential of 1.1 V. The charge transfer resistance of three samples becomes smaller after cycling due to the improvement of interface between electrode and electrolyte and the increased conductivity of electrodes by the reduction at low potentials. Among them, NbPAA-900 displays the lowest charge transfer resistance, and high ionic diffusion at low frequency ensures it provide better electrochemical performance than other samples.

To deeply understand the high-rate capability of NbPAA-900, its CV curves at various scan rates were used for investigating the reaction kinetic, which are shown in Fig. 8a. The shapes of each curve are identical with peak currents gradually increasing as scan rates ascending. The obtained b-value from anodic peaks is 0.87, as the slope of log(i) vs log(v) plot in Fig. 8b, which indicates its capacity should include both capacitive and diffusion-controlled contributions **[11, 32, 33].** And the valves of k^2 and k^2 are 0.583 and 0.115, respectively, obtained by plotting $v^{1/2}$ vs $i/v^{1/2}$. Based on the value of the valves of k^2 and k^2, the ratios of capacitive and diffusion-controlled contributions are summarized in Fig. 8c at each scan rate. At the low scan rate of 0.1 mv s^{-1}, the faradic capacity of M-Nb_2O_5 possessed more than half of the total capacity. When the scan rate increases from 0.1 to 1 mV s^{-1}, the proportion of capacitive capacity of NbO_2 and T-Nb_2O_5 reaches up to 72.3% (Fig. 7c), which means the one of M-Nb_2O_5 still have about 27.7% **[11].** The good retention of faradic capacity of M-Nb_2O_5 is due to its inherent property and high conductivity of carbon and NbO_2. Therefore, M-Nb_2O_5 in the composite of NbPAA-900 not only increase its specific capacity but also contribute to the high-rate capability. The issue of M-Nb_2O_5 is the capacity decay during the charge-discharge process.

Conclusion

In summary, we have prepared three niobium species/carbon composites by calcinating NbPAA precursor at different temperatures. It has been found that the reduction of Nb2O5 by carbon occurred above the temperature of 900 °C. Chemical compositions of these composites change, following the principle of phase transition of Nb_2O_5 and the degree of reduction with the increasing of temperature. Electrochemical performance demonstrated that NbPAA-900 can exhibit the highest specific capacity of 142 mAh g^{-1} at 0.05 A g^{-1} and best rate capacity (46.5 mAh g^{-1} at 5 A g^{-1} or 25 C) among three samples. These improved Li-storage performances come from the good conductivity of carbon matrix and NbO_2, and the large specific capacity and high-rate capability of M-Nb_2O_5. However, a slight decay of specific capacity upon the cycle times was observed due to the phase change of M-Nb_2O_5 during the lithiation and delithiation (81.6% after 200 cycles at 0.2 A g^{-1}).

References

[1] Li W, Song B, Manthiram A (2017) High-voltage positive electrode materials for lithium-ion batteries. Chem Soc Rev 46(10):3006-3059. https://doi.org/10.1039/C6CS00875E

[2] Zuo W, Li R, Zhou C, Li Y, Xia J, Liu J (2017) Battery-supercapacitor hybrid devices: recent progress and future prospects. Adv Sci 4(7):1600539. https://doi.org/10.1002/ad vs.201600539

[3] Dubal DP, Ayyad O, Ruiz V, Gomez-Romero P (2015) Hybrid energy storage: the merging of battery and supercapacitor chemistries. Chem Soc Rev 44(7):1777-1790. http s://doi.org/10.1039/C4CS00266K

[4] Li C, Zhang X, Sun C, Wang K, Sun X, Ma Y (2019) Recent progress of graphene-based materials in lithium-ion capacitors. J Phys D Appl Phys 52(14):143001. https://doi.org/10. 1088/1361-6463/aaff3a

[5] Choi HS, Park CR (2014) Theoretical guidelines to designing high performance energy storage device based on hybridization of lithium-ion battery and supercapacitor. J Power Sources 259:1-14. https://doi.org/10.1016/jjpow sour.2014.02.001

[6] Deng B, Lei T, Zhu W, Xiao L, Liu J (2018) In-plane assembled orthorhombic Nb2O5 nanorod films with high-rate Li? intercalation for high-performance flexible Li-ion capacitors. Adv Funct Mater 28(1):1704330. https://doi.org/ 10.1002/adfm.201704330

[7] Kong L, Zhang C, Wang J, Qiao W, Ling L, Long D (2015) Free-Standing T-Nb2O5/graphene composite papers with ultrahigh gravimetric/volumetric capacitance for Li-ion intercalation pseudocapacitor. ACS Nano 9(11):11200-11208. https://doi.org/10.1021/acsnano.5b04737

[8] Naoi K, Naoi W, Aoyagi S, Miyamoto J-i, Kamino T (2013) New generation 'nanohybrid supercapacitor.'' Acc Chem Res 46(5):1075-1083. https://doi.org/10.1021/ar200308h

[9] Augustyn V, Come J, Lowe MA, Kim JW, Taberna P-L, Tolbert SH, Abruna HD, Simon P, Dunn B (2013) High-rate electrochemical energy storage through Li? intercalation pseudocapacitance. Nat Mater 12:518-522. https://doi.org/ 10.1038/nmat3601

[10] Ma G, Li K, Li Y, Gao B, Ding T, Zhong Q, Su J, Gong L, Chen J, Yuan L, Hu B, Zhou J, Huo K (2016) High-performance hybrid supercapacitor based on graphene-wrapped mesoporous T-Nb2O5

nanospheres anode and mesoporous carbon-coated graphene cathode. ChemElectroChem 3(9):1360-1368. https://doi.org/10.1002/celc.201600181

[11] Lim E, Jo C, Kim H, Kim M-H, Mun Y, Chun J, Ye Y, Hwang J, Ha K-S, Roh KC, Kang K, Yoon S, Lee J (2015) Facile synthesis of Nb2O5@carbon core-shell nanocrystals with controlled crystalline structure for high-power anodes in hybrid supercapacitors. ACS Nano 9(7):7497-7505. https://doi.org/10.1021/acsnano.5b02601

[12] Yan L, Rui X, Chen G, Xu W, Zou G, Luo H (2016) Recent advances in nanostructured Nb-based oxides for electrochemical energy storage. Nanoscale 8(16):8443-8465. https://doi.org/10.1039/C6NR01340F

[13] Kim JW, Augustyn V, Dunn B (2012) The effect of crystallinity on the rapid pseudocapacitive response of Nb2O5. Adv Energy Mater 2(1):141-148. https://doi.org/10.1002/aenm.201100494

[14] Lim E, Kim H, Jo C, Chun J, Ku K, Kim S, Lee HI, Nam I-S, Yoon S, Kang K, Lee J (2014) Advanced hybrid supercapacitor based on a mesoporous niobium pentox-ide/carbon as high-performance anode. ACS Nano 8(9):8968-8978. https://doi.org/10.1021/nn501972w

[15] Yu H, Xu L, Wang H, Jiang H, Li C (2019) Nanochannel-confined synthesis of Nb2O5/CNTs nanopeapods for ultrastable lithium storage. Electrochim Acta 295:829-834. https://doi.org/10.1016/j.electacta.2018.11.017

[16] Narendar Y, Messing GL (1997) Synthesis, decomposition and crystallization characteristics of peroxo-citrato-niobium: an aqueous niobium precursor. Chem Mater 9(2):580-587. https://doi.org/10.1021/cm960407w

[17] Yerlikaya C, Ullah N, Kamali AR, Vasant Kumar R (2016) Size-controllable synthesis of lithium niobate nanocrystals using modified Pechini polymeric precursor method. J Therm Anal Calorim 125(1):17-22. https://doi.org/10.100 7/s10973-016-5336-7

[18] Kim JW, Augustyn V, Dunn B (2012) A road to environmentally friendly materials chemistry: low-temperature synthesis of nanosized K0.5Na0.5NbO3 powders through peroxide intermediates in water. Adv Energy Mater 2(1):141-148. https://doi.org/10.1002/aenm.201100494

[19] Raba AM, Bautista-Ruíz J, Joya MR (2016) Synthesis and structural properties of niobium pentoxide powders: a comparative study of the growth process. Mater Res 19(6):1381—1387. https://doi.org/10.1590/1980-5373-mr-20 15-0733

[20] Sunde TOL, Grande T, Einarsrud M-A (2016) Modified Pechini synthesis of oxide powders and thin films. In: Klein L, Aparicio M, Jitianu A (eds) Handbook of sol-gel science and technology. Springer International Publishing, Cham, pp 1—30. https://doi.org/10.1007/978-3-319-19454-7_130-1

[21] Lanfredi S, Folgueras-Dominguez S, Rodrigues ACM (1995) Preparation of LiNbO3 powder from the thermal decomposition of a precursor salt obtained by an evaporative method. J Mater Chem 5(11):1957—1961. https://doi.org/10. 1039/JM9950501957

[22] Cao J, Xiao G, Xu X, Shen D, Jin B (2013) Study on carbonization of lignin by TG-FTIR and high-temperature carbonization reactor. Fuel Process Technol 106:41—47. https://doi.org/10.1016/j.fuproc.2012.06.016

[23] Ding H, Song Z, Zhang H, Zhang H, Li X (2020) Niobium-based oxide anodes toward fast and safe energy storage: a review. Mater Today Nano 11:100082. https://doi.org/10.1016/j.mtnano.2020.100082

[24] Liao J, Tan R, Kuang Z, Cui C, Wei Z, Deng X, Yan Z, Feng Y, Li F, Wang C, Ma J (2018) Controlling the morphology, size and phase of Nb2O5 crystals for high electrochemical performance. Chin Chem Lett 29(12):1785—1790. https://d oi.org/10.1016/j.cclet.2018.11.018

[25] Park H, Lee D, Song T (2019) High capacity monoclinic Nb2O5 and semiconducting NbO2 composite as high-power anode material for Li-Ion batteries. J Power Sources 414:377-382. https://doi.org/10.1016/jjpowsour.2019.0L015

[26] Ramakrishnan S, Balamurugan J, Vinothkannan M, Kim AR, Sengodan S, Yoo DJ (2020) Nitrogen-doped graphene encapsulated FeCoMoS nanoparticles as advanced trifunctional catalyst for water splitting devices and zinc-air batteries. Appl Catal B Environ 279:119381. https://doi.org/10. 1016/j.apcatb.2020.119381

[27] Ramakrishnan S, Velusamy DB, Sengodan S, Nagaraju G, Kim DH, Kim AR, Yoo DJ (2022) Rational design of multifunctional electrocatalyst: An approach towards efficient overall water splitting and rechargeable flexible solid-state zinc-air battery. Appl Catal B Environ 300:120752. https://d oi.org/10.1016/j.apcatb.2021.120752

[28] Ramakrishnan S, Karuppannan M, Vinothkannan M, Ramachandran K, Kwon OJ, Yoo DJ (2019) Ultrafine Pt nanoparticles stabilized by MoS2/N-doped reduced graphene oxide as a durable electrocatalyst for alcohol oxidation and oxygen reduction reactions. ACS Appl Mater Interfaces 11(13):12504-12515. https://doi.org/10.1021/acsami.9b00192

[29] Shim H, Lim E, Fleischmann S, Quade A, Tolosa A, Presser V (2019) Nanosized titanium niobium oxide/carbon electrodes for lithium-ion energy storage applications. Sustain Energy Fuels 3(7):1776-1789. https://doi.org/10.1039/C9SE00166B

[30] Hu Z, He Q, Liu Z, Liu X, Qin M, Wen B, Shi W, Zhao Y, Li Q, Mai L (2020) Facile formation of tetragonal-Nb2O5 microspheres for high-rate and stable lithium storage with high areal capacity. Sci Bull 65(14):1154-1162. https://doi. org/10.1016/j.scib.2020.04.011

[31] Asfaw HD, Tai C-W, Nyholm L, Edstrom K (2017) Overstoichiometric NbO2 nanoparticles for a high energy and power density lithium microbattery. ChemNanoMat 3(9):646-655. https://doi.org/10.1002/cnma.201700141

[32] Hou T, Tang G, Sun X, Cai S, Zheng C, Hu W (2017) Perchlorate ion doped polypyrrole coated ZnS sphere composites as a sodium-ion battery anode with superior rate capability enhanced by pseudocapacitance. RSC Adv 7(69):43636-43641. https://doi.org/10.1039/c7ra07901j

[33] Boota M, Chen C, Van Aken KL, Jiang J, Gogotsi Y (2019) Organic-inorganic all-pseudocapacitive asymmetric energy storage devices. Nano Energy 65:104022. https://doi.org/10. 1016/j.nanoen.2019.104022